

Production and Characterization of a Modified Hot Work Tool Steel by Laser Powder Bed Fusion



FARAZ DEIRMINA, PAUL A. DAVIES, NIKHIL DIXIT, RAVEENDRA SIRIKI,
and MASSIMO PELLIZZARI

Conventional hot work tool steels with medium carbon content, fabricated by laser powder bed fusion (L-PBF), are susceptible to cracking. To reduce this risk, as in well-established welding process, usually preheating or in-situ heating needs to be applied. In order to address this issue, a modified grade, with lower carbon wt pct, is proposed to fabricate parts showing less susceptibility to cracking. The microstructure was studied in the as-built condition and after direct double tempering for 2 hours each at 625 °C and 650 °C. Tensile properties and hardness were compared with those of wrought and (L-PBF) processed AISI H13. The results confirm improved printing performance of the new steel grade and the possibility of achieving similar hardness and strength by proper tempering treatment.

<https://doi.org/10.1007/s11661-022-06694-2>
© Crown 2022

I. INTRODUCTION

ADDITIVE manufacturing (AM) is a fast-growing industrial technology receiving increasing attention in recent years due to the unique characteristics in the production of complex geometries in a short time and sustainable way for a variety of materials.^[1,2] Laser powder bed fusion (L-PBF) is one of the most practiced technologies for metal AM due to its distinctive capacities in manufacturing. L-PBF offers design freedom to fabricate tools with optimized design such as dies with intricate cooling channels, and forming and trimming tools.^[3,4]

AISI H13 is a Cr, Mo, V hot work tool steel which must be used in quenched and tempered condition. The steel shows a combination of high hardness and toughness after tempering at temperatures above the secondary hardening peak (*i.e.*, above 500 °C).^[5-7] This material is hard to process by L-PBF additive manufacturing due to cracking, especially in the absence of plate preheating or L-PBF chamber heating.^[6] The cracking observed in L-PBF processed AISI H13,

without using plate preheating or heated L-PBF chamber, might be explained in view of two mechanisms both related to large residual stress build-up which leads to brittle fracture in the hard martensite.

The first and most important source of residual stress is the martensitic phase transformation, occurring at around 250 °C-300 °C, which results in localized, constrained volume expansion and dramatic increase in dislocation density. By using Transmission Electron Microscopy (TEM) and high-angle X-ray diffraction measurements, Yan *et al.*^[8] quantified the large amount of martensite, and large residual stress in L-PBF-processed H13 steel. They reported that the component of martensitic transformation was the most significant factor contributing to the residual stress build-up. Through Finite Element Analysis, Deng^[9] quantified the relation between carbon content, martensitic transformation, and residual stress in laser-welding of steel. For medium-carbon steels (*e.g.*, H13), the authors showed that large residual stresses are the result of relatively large dilation and low martensite start (M_s) temperature, while in low carbon steels martensitic transformation had an insignificant effect on residual stresses because of a negligible dilation and the relatively higher transformation temperature. Murakawa *et al.*^[10] and Francis *et al.*^[11] showed that if the martensitic phase transformation temperature (*i.e.*, M_s) is lower than 400 °C, the overall residual stress can be large and compressive. In L-PBF-processed H13, processed without plate preheating, the residual stress was compressive (~ 400 MPa) due to the volume expansive martensitic transformation.^[8,12] Preheating led to the achievement of crack-free samples, and the reduction of the residual stress.^[12] Interestingly,

FARAZ DEIRMINA, PAUL A DAVIES, and NIKHIL DIXIT are with the Sandvik Additive Manufacturing AB, Mossvägen 10, 811 82, Sandviken, Sweden. Contact e-mail: Paul.a.davies@sandvik.com RAVEENDRA SIRIKI is with the AB Sandvik Materials Technology, Järnverksleden 8, 811 34, Sandviken, Sweden. MASSIMO PELLIZZARI is with the Department of Industrial Engineering, University of Trento, Via Sommarive 9, 38123, Trento, Italy.

Manuscript submitted November 2, 2021; accepted April 12, 2022.
Article published online May 5, 2022

preheating at 300 °C (*i.e.*, slightly above Ms of H13) resulted in negligible residual stress (*i.e.*, 78 MPa), while the residual stress was reported to be tensile by preheating at 400 °C, probably due to the in-situ tempering of bainite.^[12] The second source of residual stresses is the steep temperature gradients, characteristic of L-PBF process, which causes two different stress-induced mechanisms (*i.e.*, thermal gradient and volume shrinkage upon melt pool non-equilibrium rapid solidification).^[8] Both the above-mentioned factors convey the fact that increased residual stress by larger C content, local yield strength and toughness, and the local temperature gradient govern the cracking susceptibility.

Crack susceptibility due to the residual stress can be explained by the high hardness of the extremely supersaturated BCC (or BCT) martensitic matrix with limited ductility, therefore, dislocation interactions will be accompanied by the formation of immobile dislocations, crack nucleation (or crack propagation from pre-existing defects), and finally brittle fracture. Other than plate preheating to above 200 °C, and sometimes up to 400 °C (*i.e.*, to suppress martensitic transformation and reduce the thermal gradient), optimized scanning strategies have been proven to reduce steep temperature gradients significantly.^[12,13] Another approach might be the adjustment of chemical composition in a way that Ms shifts to higher temperatures to ease the accommodation of the residual stress created by the martensitic transformation. In addition to that, a chemical composition leading to higher Ms generally shows a lower hardness in quenched condition (*i.e.*, softer martensite), this plays a complementary role to increase the resistance against the brittle fracture caused by internal residual stresses. Indeed, also in welding experiments, the material with lower yield strength in quenched condition needs a lower preheating temperature. For this purpose, two main influencing factors to modify the chemistry should be considered:

Ms temperature, which can be roughly estimated using the following empirical equation, considering the wt pct of alloying elements^[14]

$$M_s(^{\circ}C) = 545 - 601.2(1 - \exp(-0.868C \text{ pct}) - 34.4Mnpct - 13.7Si \text{ pct} - 9.2Cr \text{ pct} - 17.3Ni \text{ pct} - 15.4Mo \text{ pct} + 10.8V \text{ pct} + 4.7Co \text{ pct} - 1.4Al \text{ pct} - 16.3Cu \text{ pct} - 361Nb \text{ pct} - 2.44Ti \text{ pct} \quad [1]$$

The hardness of the martensite after rapid cooling to temperatures below Ms, which can be correlated to the carbon equivalent (C_{eq}) in wt pct^[15]

$$C_{eq} = Cpct + A(C) \left[\frac{Mnpct}{6} + \frac{Crpct + Mopct + Vpct + Nbpct}{5} + \frac{Sipct}{24} + \frac{Cupct}{15} + \frac{Nipct}{20} \right] \quad [2]$$

$$A(C) = 0.75 + 0.25 \tanh[20(Cpct - 0.12)]$$

where hardness of martensite is proportional to the C_{eq} and cooling rate, v ^[16]

$$H \propto AC_{eq} + Blog(v) \quad [3]$$

Above equations suggest that the most effective way to mitigate cracking in L-PBF H13 is reduction in carbon wt pct. However, the hardness of tempered H13 tool steel is provided by the dispersion of fine secondary carbides within the relatively tough tempered martensite. Therefore, reducing C content will reduce both martensite hardness as well as carbides vol pct, with a potential negative impact on steel properties. From the work of Berns and Wendl,^[17] who studied the effect of carbon on Cr, Mo, V hot work tool steels, it was concluded that in H13 with reduced C content (*i.e.*, 0.27 wt pct vs 0.4 wt pct) the main effect is a drop in quenched hardness, as well as in the tempered condition up to the secondary hardening peak (~500 °C). However, in the technically used tempering range (*i.e.*, 575 °C to 650 °C) the difference in hardness became negligible. Accordingly, to achieve a tensile strength of 1500MPa, low carbon H13 was tempered lower than standard H13 by only 7 °C. Ms temperature was higher in the low carbon steel, and this was backed by the difference in relative change in length during martensitic transformation which led to reduced size distortion of low carbon H13 upon quenching. In addition to that, Norström^[18] clearly showed that by the incorporation of higher Mo, and lowering Cr in hot work tool steels, the tempering resistance was significantly improved, as the consequence of the higher coarsening resistance of Mo-rich (e.g., M_6C or M_2C) compared with Cr-rich ($Cr_{23}C_6$) carbides. In fact, about 3 wt pct Cr was enough to ensure optimum oxidation and hardness properties. Finally, small additions of Co could increase the hot hardness of the steel as well as the Ms temperature, which can be used as an additional factor in producing crack-free hot work tool steels by L-PBF technique.

The aim of the present work is to evaluate the properties of a new hot work tool steel grade with lower C, increased Mo, and reduced Cr content than AISI H13. This study focuses on tensile properties and hardness of the modified steel.

II. MATERIALS AND METHODS

The compositions of the new experimental steel powder (herein after H13-Mod) and that of standard AISI H13 are listed in Table I.

Spherical inert gas atomized powders with a particle size distribution of ($-53 \mu\text{m} + 15 \mu\text{m}$) were used. For both materials, builds were performed in an EOS M290 machine equipped with 400 W Yb-fiber laser. The build plate was heated to 80 °C and the build was conducted in nitrogen atmosphere. Laser beam size was 80 μm , hatching distance was set to 0.11 mm, and layer thickness to 40 μm . Stripes were used as a scan pattern with stripe width of 5 mm. The scan pattern was rotated

Table I. Chemical Composition of the Starting Powders

| Element Wt Pct | C | Si | Mn | Cr | Mo | V | Ti | Fe |
|----------------|-----------|-----|------|---------|---------|---------|------------|------|
| H13-Mod | 0.25-0.30 | 0.7 | 0.3 | 3.0-4.0 | 2.0-2.8 | 0.5-0.7 | 50-200 ppm | bal. |
| H13 | 0.4 | 1.0 | 0.35 | 5.1 | 1.5 | 1.0 | — | bal. |

67 degrees between layers. For the process optimization, the widely used volumetric laser energy density (E) was used (Eq. [4]).

$$E\left(\frac{J}{mm^3}\right) = \frac{P}{v \times h \times t}, \quad [4]$$

where P is laser power (W), v is the scanning speed (mm/s), h is the hatch spacing (mm), and t is layer thickness (mm).

Relative density measurements were carried out using image analysis on light optical microscope (LOM) images of ground and oxide polished (colloidal silica suspension, $0.02\mu\text{m}$) metallographic cross sections. High-resolution field emission gun scanning electron microscope (FEG-SEM) was used for the microstructural analysis. Energy-Dispersive X-ray Spectroscopy (EDXS), a semi-quantitative analysis, was used to determine the chemical compositions of different phases. Electron backscattered diffraction (EBSD) analysis was carried out using Symmetry to reveal the presence and position of retained austenite (RA) in the as-built microstructures. Vickers hardness (HV1 and HV5) measurements were carried out according to ASTM E92-82(2003). Tensile tests were performed conforming to ASTM E8M on small size specimens. Three samples were tested for each orientation (*i.e.*, tensile loading normal to build direction (BD), and parallel to BD). The test was displacement-controlled, strain rate was 0.00025 s^{-1} up to $\sim \epsilon = 1.7$ pct and changed to 0.0067 s^{-1} until fracture. Thermodynamic simulations were carried out using Thermo-Calc software (2021a, TCFE11 database).

Samples were double tempered directly from the as-built condition either at $625\text{ }^\circ\text{C}$ or $650\text{ }^\circ\text{C}$ for 2 h. These two tempering temperatures are common tempering temperatures for the H13 tool steel according to the use of mold or die.^[19] Tempering was performed in a chamber furnace followed by air cooling. After tempering, samples were cut from the build plate by electro discharge machining (EDM).

III. RESULTS AND DISCUSSION

A. Rel. Density, Microstructure, and Hardness of the As-Built Parts

The optical micrograph of metallurgical cross sections confirmed that it was difficult to produce crack free, near fully dense test cubes in H13 even by selecting suitable parameters using process optimization (Figures 1(a) and (c)). However, in the case of H13-Mod no cracks and near full density (*i.e.*,

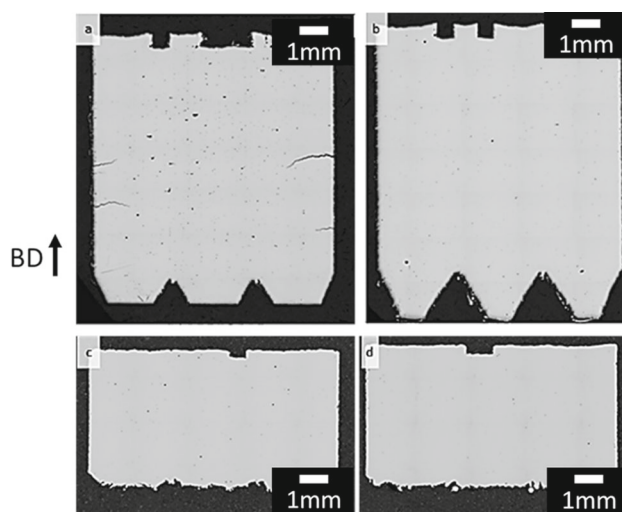


Fig. 1—Results from process optimization (a) H13 showing cracks ($E \sim 67\text{ J/mm}^3$), (b) H13-Mod without cracks ($E \sim 67\text{ J/mm}^3$), (c) H13 with -0.6 pct porosity ($E \sim 80\text{ J/mm}^3$), and (d) near fully dense H13-Mod ($E \sim 80\text{ J/mm}^3$).

Table II. Hardness and Rel. Density of the Samples

| | Rel. Density (pct) | Hardness (HV1) |
|---------|--------------------|----------------|
| H13 | 99.8 | 668 ± 4 |
| H13-Mod | 99.9 | 516 ± 11 |

99.9 pct) were observed by optimized laser energy density (Figures 1(b) and (d)). The as-built hardness of H13 and H13-Mod were 668 ± 4 HV1 and 516 ± 11 HV1, respectively (Table II), in agreement with the lower C content in H13-Mod leading to a softer martensite.

Similar to other works,^[3,8,13] the as-built L-PBF H13 showed a mainly martensitic microstructure. The solidification structure was cellular/dendritic (Figure 2(a)), with the heavy micro-segregation of carbon and other alloying elements (*i.e.*, Mo, V, and Cr) to the cellular boundaries (Figures 2(b), (c) and Table III) as a result of the fast, non-equilibrium solidification, characteristics of L-PBF process. Some evidence of Mo/V-rich carbide precipitation could be found at cell boundaries (Figure 2(c)). Similar features were also found for H13-Mod (Figure 2(d)) showing an apparently larger number of carbides at the intercellular areas (Figure 2(e)).

EBSD results confirmed the presence of retained austenite (RA) in the as-built H13 (Figures 3(a), (b)), RA was mainly located at cell/dendrite boundaries in the as-built H13 microstructure (Figures 3(c), (d)), in

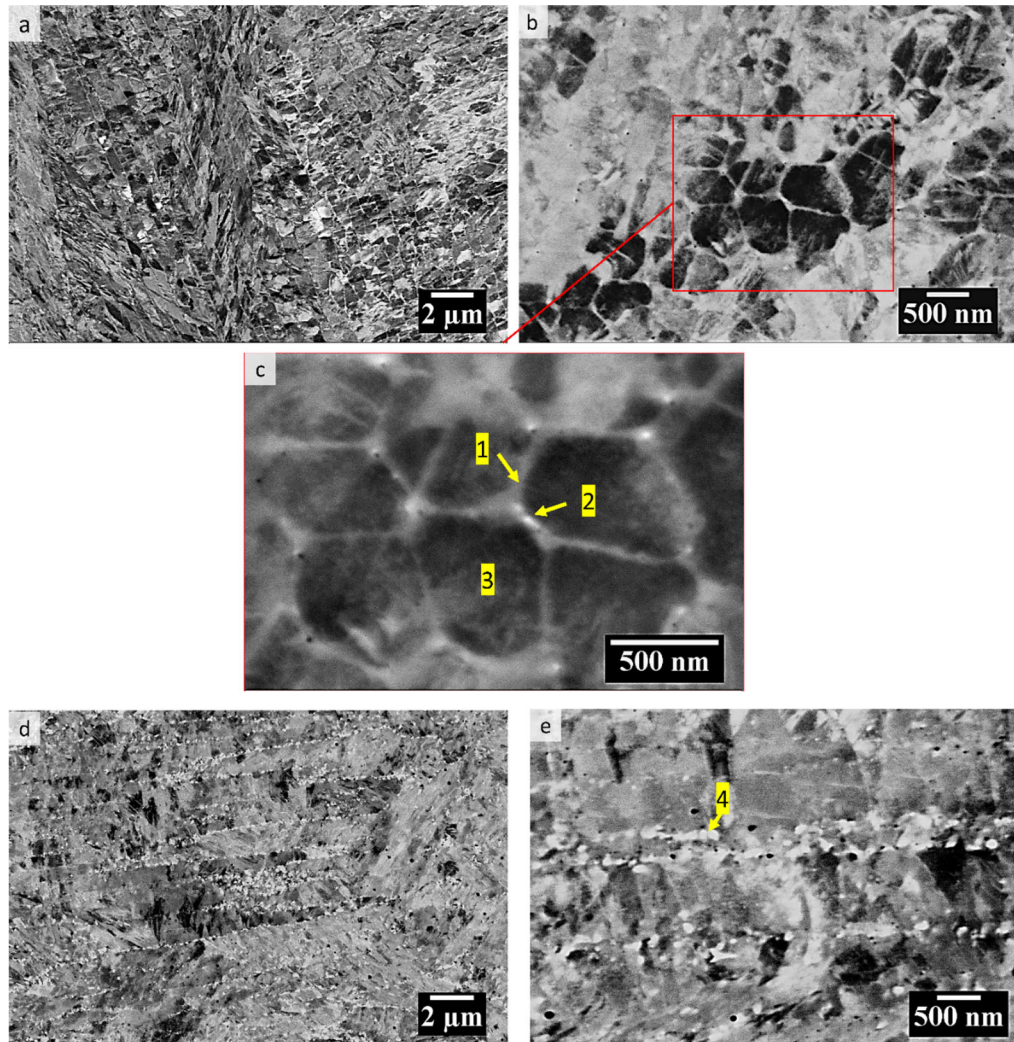


Fig. 2—SEM micrographs, (a) H13 tool steel showing a martensitic microstructure with the cellular/dendritic solidification structure, (b) cellular structure in H13 tool steel, (c) a higher magnification micrograph showing intercellular micro-segregation and particles at cells boundary of H13, (d) H13-Mod martensitic microstructure with the cellular/dendritic solidification structure, and (e) a higher magnification micrograph showing intercellular micro-segregation in H13-Mod.

line with the previous work of authors.^[20] In fact, in an austenitized and quenched H13, RA was reduced to less than 2 pct, suggesting that the large amount of RA in L-PBF H13 can be explained by its chemical stabilization caused by micro-segregation (*i.e.*, local enrichment of the alloying elements) at the cell/dendrite boundaries, because of rapid solidification (Table III). The local increase in austenite stability is coherent with the lower M_s temperature at those areas.^[20–22] Considerably lower amount of RA was found in the as-built H13-Mod (Figures 3(e), (f)), which can be a result of lower C wt pct in H13-Mod (see Eq. [1]). The RA content in H13 was around 11 vol pct (Figure 3(b)), while this amount was reduced to ~ 2 vol pct in H13-Mod (Figure 3(f)). These measurements can only be used as a rough estimation, due to the very fine size of intercellular RA (*i.e.*, ~250 nm) in laser-based AM steels,^[23] which can lead to measurement uncertainties by using low-magnification EBSD scans with coarse step sizes.^[24] For a more precise evaluation, higher magnification scans, and

step sizes of ~ 50 nm, with sufficient sampling would be needed. Present results are then useful to demonstrate the lower RA formation tendency of H13-Mod. For the purpose of comparison, the reported RA vol pct, using X-ray diffraction (XRD) analysis, in L-PBF H13 was around 19 pct in the previous work of the authors.^[20]

To get an insight to the rapid solidification behavior and phase constitution of the samples, thermodynamic modeling was considered. The Scheil solidification model (Figure 4(a)) can be used for multicomponent systems. The model involves complete diffusion in the liquid phase while no diffusion in the solid phase is allowed, and that local equilibrium holds at the liquid/solid interface. Moreover, using Thermo-Calc software, it was possible to account for solute trapping in Scheil model specifically developed for AM simulations. The solidification speed (V_s) was calculated by using the laser scanning speed (v) set to 980 mm/s, and the angle between solid/liquid interface and scanning direction (α) set as default (*i.e.*, 45 deg), through Eq. [5].

Table III. Wt Pct of Cr, Mo, and V by EDS Analysis on Marked Areas in Figs. 2(c) and (e), Matrix Composition is Reported for Comparison

| Point | Region | Cr Wt Pct | Mo Wt Pct | V Wt Pct |
|-------|--|-----------|-----------|----------|
| 1 | cellular boundaries | 6.1 | 2.8 | 1.5 |
| 2 | particles at the cell boundaries | 6.6 | 3.8 | 3.1 |
| 3 | H13 Matrix | 4.8 | 1.3 | 1.2 |
| 4 | particles at interdendritic areas, H13-Mod | 5.7 | 6.5 | 1.0 |

$$V_s \left(\frac{mm}{s} \right) = v \times \alpha \quad [5]$$

The liquidus temperature of H13-Mod. is slightly higher than that of H13 due to the lower C content and the lower wt pct of alloying elements. In all calculations, delta ferrite, *i.e.*, the first solid phase to form, was removed from the calculations, and austenite is the first solid phase to form. The elimination of delta ferrite was because there were no traces of delta ferrite in the as-built microstructure. This was backed by the pioneering work of Chou *et al.*^[21] arguing that, at high solidification velocities, austenite dendrite tip temperature is higher than that of delta ferrite. Therefore, at extremely high solidification rates (e.g., L-PBF), austenite is more likely to form. In both cases, the deviation from equilibrium solidification (onset of micro-segregation in these systems) happens at around 0.45 mole fraction of liquid to solidify. The Scheil model predicts the precipitation of M_7C_3 , and MC-type carbides from the last liquid fraction (*i.e.*, at the cellular boundaries) in H13, in line with a recent work of Casati *et al.*^[25] on L-PBF X38CrMoV5-1 hot work tool steel. While formation of M_6C carbides from the heavily alloyed liquid is predicted in H13-Mod. This is justified by the lower C and V activities and the higher activity of Mo in H13-Mod. According to the calculations, MC carbides are rich in V and Mo (*i.e.*, 67 wt pct and 12 wt pct, respectively) in H13, while in H13-Mod, Mo concentration in M_6C carbides is 49 wt pct and V is reduced to 6 wt pct. This is fairly in line with the semi-quantitative EDS analysis (Table III).

The micro-segregation of alloying elements associated with fast solidification is depicted in Figures 4(b) and (c) for H13 and H13-Mod, respectively. By increasing the solid fraction, the amount of C and alloying elements inside the remaining liquid increases. To estimate the effect of cell boundary micro-segregation on chemical stabilization of RA, the chemical composition of solid phase *vs* temperature, up to 0.02 mass fraction of liquid to solidify, (*i.e.*, Figures 4(b), (c)) was considered. It must be pointed out that Scheil model is often used for fast non-equilibrium solidification modeling due to the simplicity of its use. However, important parameters, such as the cut-off limit of the residual liquid amount, and temperature step size might impose significant differences in the calculation results. Therefore, this might result in errors in the predicted mass fraction of eutectic phases forming at the end of the solidification. In the current work, the temperature step size was selected as the default value (*i.e.*, 1), and due to the comparative nature of the

current study, lower step sizes which need larger simulation times and cost were not tried.^[26]

Assuming no further homogenization upon extremely fast cooling, down to the martensite start temperature, the chemical composition profiles were used as the input for the empirical Ms equation (see Eq. [1]). The results are shown in Figure 4(d). According to calculations, the Ms temperature of the intercellular austenite formed at the end of solidification becomes lower than the room temperature (RT) due to the local enrichment of alloying elements. This confirms the stabilization of RA at those regions. The Ms profile calculated by Eq. [1] shows a fairly similar trend in comparison to that calculated as a function of segregation profile, using more precise computational thermodynamic considerations by taking the cooling rate into account on an 0.35 wt pct C, Cr, Mo, V hot work tool steel processed by L-PBF.^[21]

The minimum Ms temperature as well as nominal one is higher in the case of H13-Mod compared with H13 due to the lower C and Cr content. The higher Ms temperature in the micro segregated areas of H13-Mod might result in less chemically stabilized RA, as confirmed by the EBSD observations (Figure 3(f)). Another plausible factor might be the increased concentration of Mo at the cellular boundaries in the H13-Mod giving rise to the precipitation of higher wt pct of carbides at those areas (Figures 2(d) and (e)) leading to depletion of Mo and C in austenite, its destabilization, and its transformation into martensite upon cooling. The higher Ms temperature as well as softer martensite in H13-Mod (Table II) are very good premises for lower residual stresses after L-PBF, and lower susceptibility to cold cracking in comparison to H13.

Apart from considerations on cold cracking, it must be noted that, by increasing the C content, solidification cracking susceptibility increases in tool steels, Xia and Kou,^[27] in their welding experiments, reported that the susceptibility index shows a minimum at C wt pct of ~ 0.2 and increases rapidly by increasing the C wt pct. The much finer dendrite/cell size in L-PBF processing than in welding process, and the lower C content in H13-Mod compared with H13 might result in lower solidification cracking susceptibility for the proposed alloy.

IV. POST PROCESSING THERMAL TREATMENTS

The hardness of the samples after double tempering at 625 °C and 650 °C is reported in Table III. As expected,

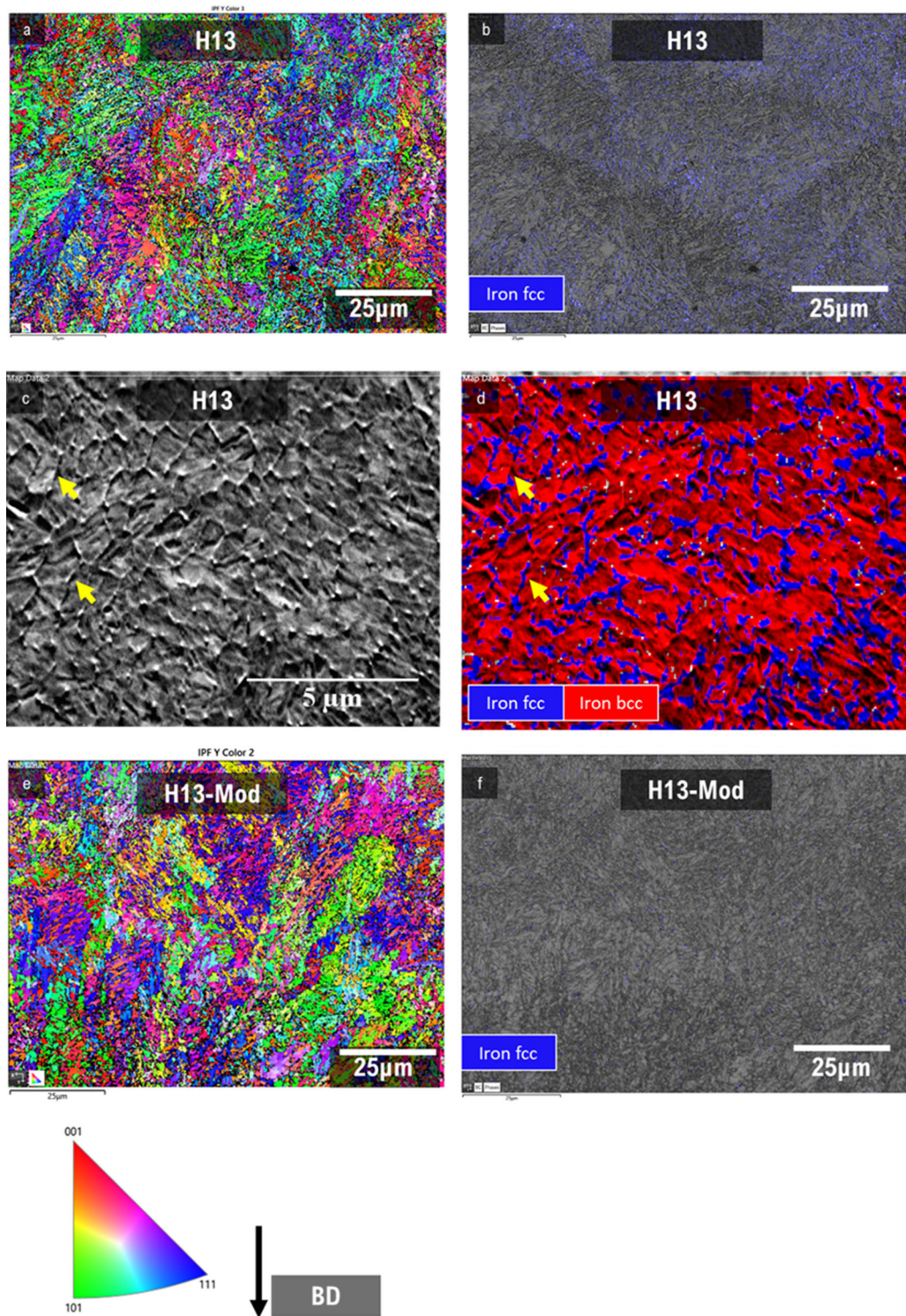


Fig. 3—As-built samples, (a) EBSD inverse pole figure (IPF) map with respect to the BD (H13), (b) corresponding band contrast image overlaid by austenite phase in blue (H13), (c) higher magnification EBSD scan for H13: Fore scattered image revealing cell boundaries, (d) corresponding band contrast image overlaid by phases (martensite in red and austenite in blue), (e) EBSD IPF map with respect to the BD (H13-mod), and (f) corresponding band contrast image overlaid by austenite phase in blue (H13-mod), note significantly lower RA in H13-Mod (Color figure online).

the hardness of H13 is higher than that of H13-Mod. However, as also shown in the work of Berns and Wendl, this difference becomes negligible at higher tempering temperature.^[17]

The reason may be found considering the most important parameters affecting secondary hardening of hot work tool steel during tempering, *i.e.*, (i) the fraction of secondary carbides, (ii) the hardness of secondary

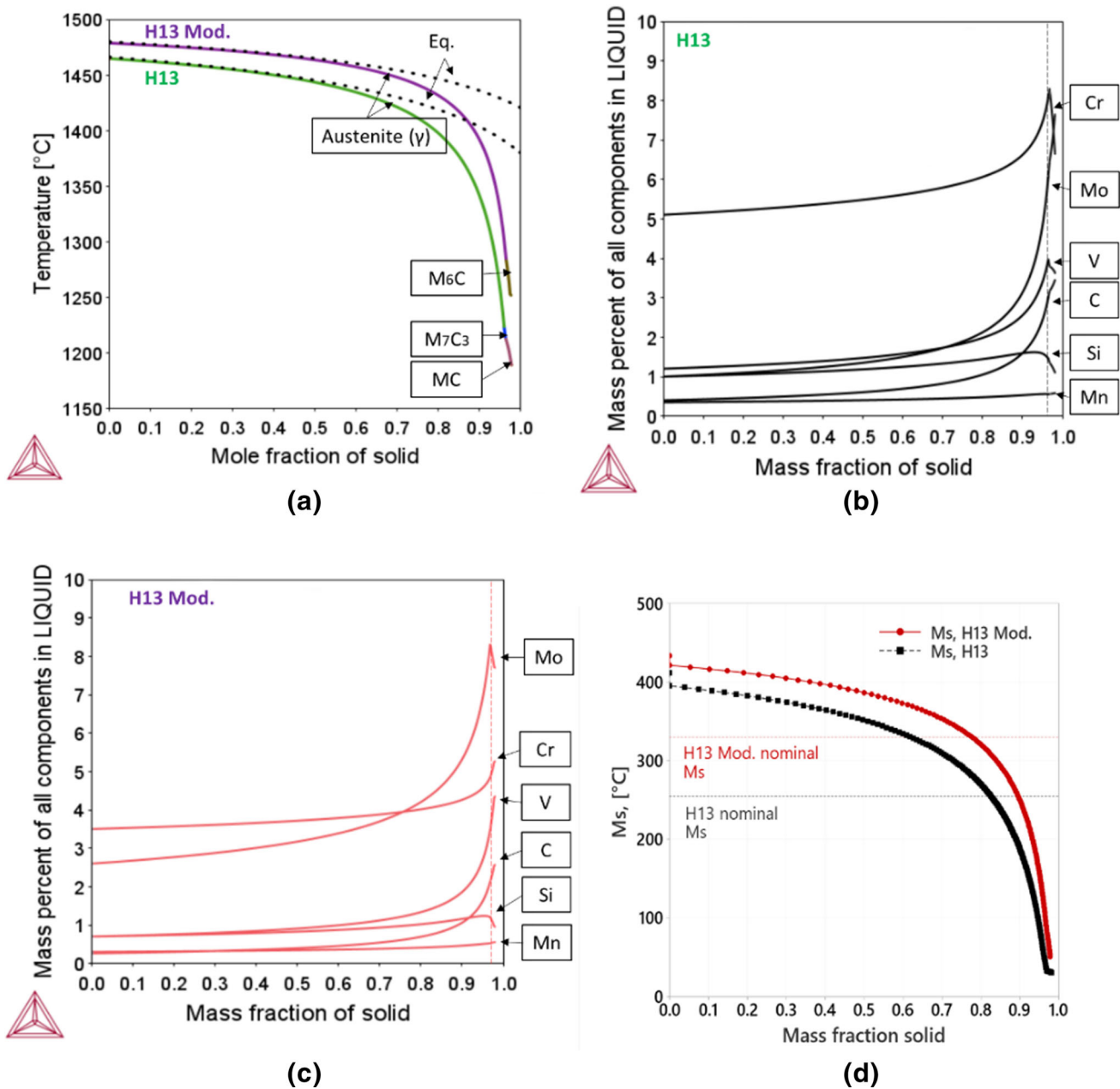


Fig. 4—(a) Scheil simulations for H13 and H13-Mod (please note that delta ferrite is removed from calculations, (b) composition of liquid phase vs mole fraction of solid (H13), (c) composition of liquid phase vs mole fraction of solid (H13-Mod), and (d) Ms mapping of local austenite composition vs mass fraction of solid.

carbides, and (iii) their resistance to coarsening at the tempering temperature. The latter two factors are mostly related to the carbide type. The higher fraction and the finer carbide size provide greater strengthening.^[28,29] For this purpose, the equilibrium property diagrams of the H13, and H13-mod within the tempering temperature range are calculated and shown in Figures 5(a), and (b), respectively. Even if these calculations show the phase fractions under equilibrium condition, they still can be useful for a qualitative comparison. The simulation results show that the overall vol pct of carbides are higher in H13 steel compared with H13-Mod (Figure 5(c)) due to the higher

C content of the former. Calculation clearly shows that the vol pct of Mo-rich carbides (e.g., M_6C and M_2C) is higher in H13-Mod than in H13, while Cr-rich carbides (e.g., $M_{23}C_6$) prevail in H13.

The $M_{23}C_6$ carbides are reported to be larger than other carbides at any tempering temperature.^[28] Moreover, the coarsening rate of this carbides, especially at temperature higher than 650 °C, is reported to be much higher than other carbides, which leads to a larger drop in hardness. Mo rich (*i.e.*, M_2C , M_6C), and (V, Mo) rich MC-type carbides are more resistant to coarsening^[30] and considered as fine and stable carbides. The M_6C carbide has the highest resistance to coarsening,

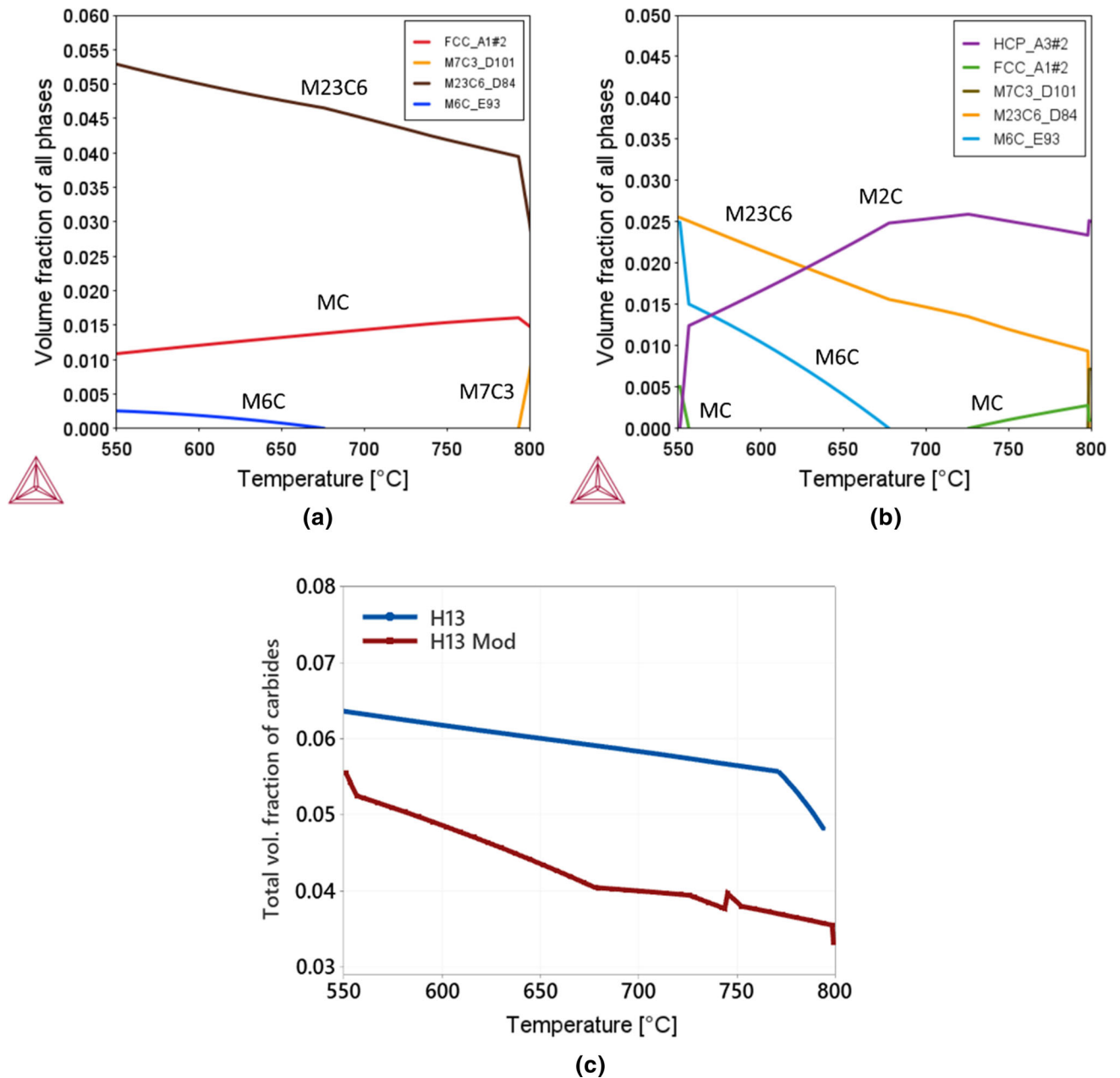


Fig. 5—Equilibrium property diagrams of (a) H13 and (b) H13-Mod at the tempering temperature range, and (c) cumulative volume fraction of carbides.

especially at elevated temperatures.^[28] Therefore, the larger vol pct of fine Mo-rich secondary carbides in H13-mod (*i.e.*, higher number density of Mo-rich carbides) might explain the smaller drop in hardness after tempering at temperatures higher than the secondary hardness peak, where recovery of dislocations, reduction in dislocation density, and carbide coarsening occur more readily. In fact, in spite of lower C content, the hardness of both steels in the technically used tempering range is almost identical (Table IV). The hardness reported here for direct tempering from the as-built condition is generally higher compared with that of quenched and tempered counterpart, possible explanations are discussed in detail in previous work of the

authors and other researchers pointing at the positive effect of decomposition of RA during the first tempering cycle.^[13,20]

The microstructure of the H13-Mod tempered at 650 °C is depicted in Figure 6. The microstructure comprises tempered martensite, strengthened by the dispersion of alloy carbides. While part of fine carbides is evenly distributed within the matrix (arrow in Figure 6(a)), an interconnected network of carbides is evident in the microstructure (arrow in Figure 6(b)), contouring the prior cellular/dendritic boundaries (see Figure 2). The higher concentration of alloying elements in those areas gave rise to the precipitation of carbides from either martensite or RA during tempering. To

eliminate this feature, an austenitizing and quenching treatment prior to tempering is necessary^[13] which is out of the scope of the present work. A higher magnification SEM micrograph (inset in Figure 6(b)) shows the presence of coarse Cr-rich carbides (1) with composition (17.3 pct Cr, 3.8 pct Mo, 2.4 pct V, 15.5 pct C (qualitative), Fe-Bal, at pct) according to semi-quantitative EDS spot analysis, while finer rod-shaped precipitates (2), which were hard to be characterized by EDS analysis due to a very fine thickness, could be Mo-rich M_2C carbides.

The tensile test curves of H13-Mod (tempered at 650 °C) are shown in Figure 7. Both, horizontally (H) (*i.e.*, tensile loading normal to BD), and vertically (V) (*i.e.*, tensile loading parallel to BD) built samples, show a yield strength of ~1500 MPa, a tensile strength of ~1670 MPa, and 6 to 7.5 pct fracture elongation. For comparison, literature data for the conventionally produced and additively manufactured H13 are presented in Table V. It can be postulated that H13-Mod, with improved L-PBF processability, meets the strength and hardness requirements of H13 applications (e.g., hot stamping, extrusion dies, or die casting dies). Of course, even if present results highlight a very high potential for the new modified H13 hot work tool steel grade, other important properties such as impact toughness, tempering resistance, thermal fatigue resistance, and tribological properties need to be assessed for a more complete validation.

V. CONCLUSIONS

To improve the L-PBF processability of H13 hot work tool steel, a new experimental grade with lower C (*i.e.*, 0.25-0.30 wt pct), slightly lower Cr (~3.0 wt pct), lower V (*i.e.*, 0.5 wt pct), and increased Mo content (*i.e.*,

Table IV. Hardness vs Tempering Temperature of the Samples (Direct Tempering)

| Tempering Temperature (2 x 2h) | 625 °C | 650 °C |
|--------------------------------|-----------|-----------|
| H13 | 560±5 HV5 | 495±4 HV5 |
| H13-Mod | 525±7 HV5 | 490±5 HV5 |

2.0-2.8 wt pct) was proposed, and its properties were reported. The main conclusions are as follows:

1. Both H13 and the modified composition were characterized by a cellular dendritic solidification structure, comprising an ultrafine martensitic matrix, and the micro-segregation of alloying elements to the cellular/dendritic boundaries. The micro-segregation resulted in the stabilization of RA, and the RA fraction in modified H13 (~2 pctvol) was lower than that of H13 (~11 pctvol), most likely due to the lower C wt pct of the former.
2. Printability of H13-Mod. was improved compared with the standard H13 because of the softer martensite achieved in the as-built condition (516 HV1 for H13-Mod., 668 HV1 for H13), and the higher Ms temperature. These properties could reduce the risk of cracking by facilitating the stress accommodation resultant of the volume expansive martensite transformation.
3. After direct tempering from the as-built condition, the hardness, and tensile properties of the experimental tool steel, in the technically significant tempering range (*i.e.*, above 575 °C), were similar to those of H13 (yield strength of 1500 MPa and a

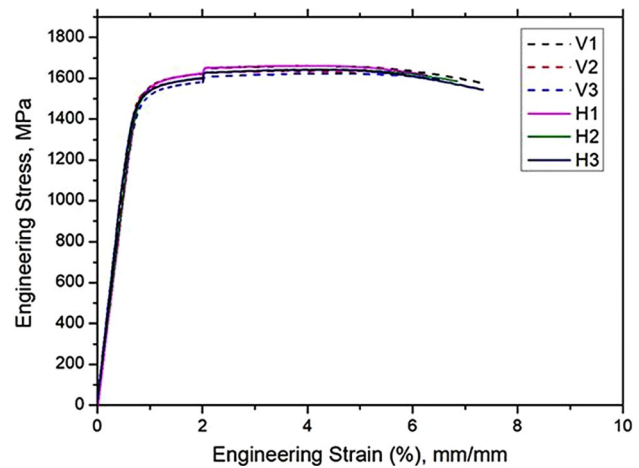


Fig. 7—Stress–Strain curves for H13-mod., tempered samples (2x-2h-650 °C), please note the change in strain rate at $\epsilon = 1.7$ pct.

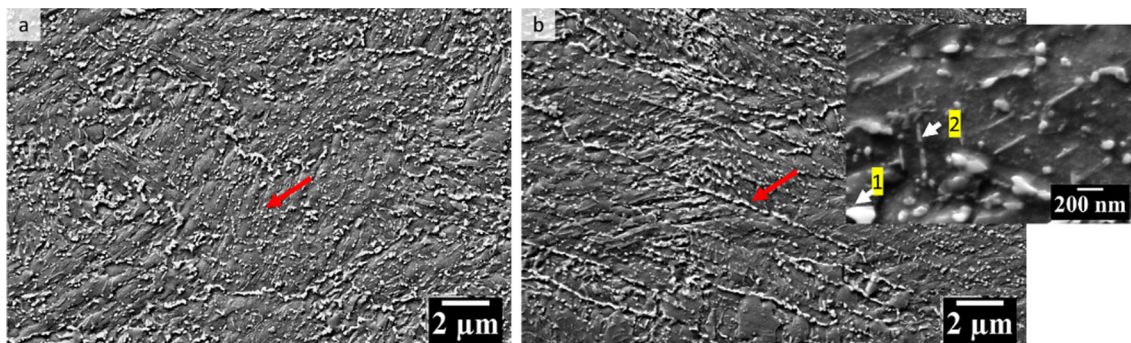


Fig. 6—SEM micrographs of tempered (2x-2h-650 °C), (a) interconnected carbide network and (b) precipitation of carbides at the intercellular/interdendritic regions, inset: a higher magnification micrograph showing carbide types with different morphologies.

Table V. A Summary of Hardness and Tensile Properties of Conventionally Produced and Additively Manufactured H13 Tool Steel

| | Austenitization | Tempering Temperature (°C) | Hardness (HV) | Yield Strength (MPa) | Elongation (Pct) | Ref. |
|---------------|-----------------|----------------------------|---------------|----------------------|------------------|-----------|
| H13 wrought | Yes | 575 | 550 | 1520 | — | [31] |
| H13 wrought | Yes | 620 | 450 | 1280 | | [31] |
| H13 wrought | Yes | — | 430 | 1340-1380 | 13.0-18.0 | [32] |
| H13 wrought | Yes | — | 460 | 1230 | 6.5 | [33] |
| H13 L-PBF | No | 650 | 511 | 1450 | 3.3 | [6] |
| H13 L-PBF | HIPped (yes) | 585 | 562 | 1500 | 6.6 | [6] |
| H13 L-PBF | No | 600 | 629 | 1483 | 5.8 | [34] |
| H13-Mod L-PBF | No | 650 | 490 | 1500 | 6.0-7.5 | this work |

fracture elongation of 6.0-7.5 pct). This was a result of increased Mo content giving rise to the precipitation of fine and stable Mo-rich secondary carbides with higher resistance to coarsening compared with the Cr-rich $M_{23}C_6$ carbides. The change in carbide morphology and size could compensate for the lower C wt pct in modified H13 from a tempering hardness viewpoint.

- Present study confirms the improved processability of the new steel grade through laser powder bed fusion. However, dealing with tools with complex geometries where sharp edges or corners, serving as stress concentrators, might reduce the resistance to cracking the suitability of present grade should be further investigated. Nevertheless, a full validation will be possible only after a more complete characterization activity aimed at determining tempering resistance, impact toughness, tribological properties, and thermal fatigue resistance.

CONFLICT OF INTEREST

On behalf of all authors, the corresponding author states that there is no conflict of interest.

REFERENCES

- N. Haghdad, M. Laleh, M. Moyle, and S. Primig: *J Mater Sci.*, 2021, vol. 56, pp. 64–107.
- S. Ford and M. Despeisse: *J. Clean. Prod.*, 2016, vol. 137, pp. 1573–87.
- P. Bajaj, A. Hariharan, A. Kini, P. Kürnsteiner, D. Raabe, and E.A. Jäggle: *Mater. Sci. Eng. A.*, 2020, vol. 772, p. 138633.
- T. Skaare and N. Asnafi: *IOP Conf. Ser.: Mater. Sci. Eng.*, 2020, vol. 967, p. 012040.
- M. Pellizzari, B. AlMangour, M. Benedetti, S. Furlani, D. Grzesiak, and F. Deirmina: *Theoret. Appl. Fract. Mech.*, 2020, vol. 108, pp. 102634–39.
- M. Åsberg, G. Fredriksson, S. Hatami, W. Fredriksson, and P. Krakhmalev: *Mater. Sci. Eng. A.*, 2019, vol. 742, pp. 584–89.
- J. Sjöström and J. Bergström: *J. Mater. Process. Technol.*, 2004, vol. 153–154, pp. 1089–96.
- J.J. Yan, D.L. Zheng, H.X. Li, X. Jia, J.F. Sun, Y.L. Li, M. Qian, and M. Yan: *J. Mater. Sci.*, 2017, vol. 52, pp. 12476–85.

- D. Deng: *Mater. Des.*, 2009, vol. 30, pp. 359–66.
- H. Murakawa, M. Béreš, C.M. Davies, S. Rashed, A. Vega, M. Tsunori, K.M. Nikbin, and D. Dye: *Sci. Technol. Weld. Join.*, 2010, vol. 15, pp. 393–99.
- J.A. Francis, H.J. Stone, S. Kundu, H.K.D.H. Bhadeshia, R.B. Rogge, P.J. Withers, and L. Karlsson: *J. Pressure Vessel Technol.*, 2009, vol. 131, pp. 041401-041401–8.
- R. Mertens, B. Vrancken, N. Holmstock, Y. Kinds, J.-P. Kruth, and J. Van Humbeeck: *Phys. Proc.*, 2016, vol. 83, pp. 882–90.
- J. Krell, A. Röttger, K. Geenen, and W. Theisen: *J. Mater. Process. Technol.*, 2018, vol. 255, pp. 679–88.
- D. Barbier: *Adv. Eng. Mater.*, 2014, vol. 16, pp. 122–27.
- N. Yurioka: *ISIJ Int.*, 2001, vol. 41, pp. 566–70.
- J.C. Ion, K.E. Easterling, and M.F. Ashby: *Acta Metall.*, 1984, vol. 32, pp. 1949–62.
- H. Berns and F. Wendl: *Steel Res.*, 1986, vol. 57, pp. 671–76.
- L.-Å. Norström, M. Svensson, and N. Öhrberg: *Met. Technol.*, 1981, vol. 8, pp. 376–81.
- R. Rodríguez-Baracaldo, J.A. Benito, E.S. Puchi-Cabrera, and M.H. Staia: *Wear.*, 2007, vol. 262, pp. 380–89.
- F. Deirmina, N. Peghini, B. AlMangour, D. Grzesiak, and M. Pellizzari: *Mater. Sci. Eng. A.*, 2019, vol. 753, pp. 109–21.
- C.-Y. Chou, N.H. Pettersson, A. Durga, F. Zhang, C. Oikonomou, A. Borgenstam, J. Odqvist, and G. Lindwall: *Acta Mater.*, 2021, vol. 2021, p. 117044.
- E.A. Jäggle, P.-P. Choi, J.V. Humbeeck, and D. Raabe: *J. Mater. Res.*, 2014, vol. 29, pp. 2072–79.
- S. Amirabdollahian, F. Deirmina, M. Pellizzari, P. Bosetti, and A. Molinari: *Mater. Sci. Eng. A.*, 2021, vol. 814, p. 141126.
- Y. Zhang, P. Lai, H. Jia, X. Ju, and G. Cui: *Metals.*, 2019, <https://doi.org/10.3390/met9010094>.
- G. Carasi, B. Yu, E. Hutten, H. Zurob, R. Casati, and M. Vedani: *Metall. Mater. Trans. A.*, 2021, vol. 52A, pp. 2564–75.
- Y.-Z. Zhao, Y.-H. Zhao, Q. Li, S.-L. Chen, J.-Y. Zhang, and K.-C. Chou: *Intermetallics.*, 2009, vol. 17, pp. 491–95.
- C. Xia and S. Kou: *Metall. Mater. Trans. B.*, 2021, vol. 52B, pp. 460–69.
- A. Eser, C. Broeckmann, and C. Simsir: *Comput. Mater. Sci.*, 2016, vol. 113, pp. 280–91.
- F. Deirmina and M. Pellizzari: *Mater. Sci. Eng. A.*, 2019, vol. 743, pp. 349–60.
- Development of hot-work tool steel for high-temperature applications: *Metals Technol.*, 2020, <https://doi.org/10.1179/030716981803275857>.
- https://www.uddeholm.com/files/PB_orvar_supreme_english.pdf.
- T. Okuno: *Trans. Iron Steel Inst. Jpn.*, 1987, vol. 27, pp. 51–59.
- G. Telasang, J.D. Majumdar, G. Padmanabham, and I. Manna: *Mater. Sci. Eng. A.*, 2014, vol. 599, pp. 255–67.
- J. Yan, H. Song, Y. Dong, W.-M. Quach, and M. Yan: *Mater. Sci. Eng. A.*, 2020, vol. 773, pp. 138845–49.

Publisher's Note Springer Nature remains neutral with regard to jurisdictional claims in published maps and institutional affiliations.